SCIENCE CHINA
Information Sciences

• RESEARCH PAPER •

February 2025, Vol. 68, Iss. 2, 120401:1–120401:10
https://doi.org/10.1007/s11432-024-4215-2

From CAS & CAE Members

Multi-wavelength plasmonic optoelectronic memristor for reconfigurable logic operations and mixed-color pattern recognition

Jiaqi HAN[1†], Zhuangzhuang LI[1†], Tao ZENG[2], Xuanyu SHAN[1], Riya SU[1], Ya LIN[1], Zhongqiang WANG[1*], Xiaoning ZHAO[1], Shencheng FU[1], Haiyang XU[1] & Yichun LIU[1*]

[1]*Key Laboratory for UV Light-Emitting Materials and Technology (Northeast Normal University), Ministry of Education, Changchun 130024, China*
[2]*Department of Materials Science and Engineering, National University of Singapore, Singapore 117575, Singapore*

Received 10 October 2024/Revised 30 October 2024/Accepted 7 November 2024/Published online 18 December 2024

Abstract Optoelectronic memristors have emerged as promising hardware platforms for highly efficient image perception owing to their low crosstalk, fast response, and low power consumption. However, the development of optoelectronic memristors with multi-wavelength recognition capabilities remains constrained by the limitations of their inherent bandgap. In this work, a multi-wavelength-modulated optoelectronic memristor that operates based on the localized surface plasmon resonance effect is developed using silver (Ag)-titanium dioxide (TiO_2)/polymethyl methacrylate (PMMA) nanocomposites. The SET voltage can be gradually reduced by modulating the optical wavelength of visible irradiation. On this basis, reconfigurable IMP and False logic operations have been implemented in the memristive logic circuit. The neuromorphic visual preprocessing and recognition function for mixed-color patterns is demonstrated based on wavelength-dependent resistive switching behaviors. The proposed optoelectronic memristor enables high-density storage and in-memory computing.

Keywords optoelectronic memristor, localized surface plasmon resonance, multi-wavelength, resistive switching, color pattern recognition

Citation Han J Q, Li Z Z, Zeng T, et al. Multi-wavelength plasmonic optoelectronic memristor for reconfigurable logic operations and mixed-color pattern recognition. Sci China Inf Sci, 2025, 68(2): 120401, https://doi.org/10.1007/s11432-024-4215-2

1 Introduction

With the rapid advancements in big data and artificial intelligence, devices based on the traditional von Neumann architecture are suffering from significant data delay and power consumption problems, mainly because of the separated storage and processing units [1–4]. Emerging neuromorphic devices have attracted great attention for emulating brain functions, such as learning and memory, exhibiting the potential to overcome the bottleneck observed in conventional devices [5–8]. Furthermore, memristors are considered the core foundation of neuromorphic computing hardware implementation because of their simple structure, fast response speed, low power consumption, and high data retention ability [9–12]. In particular, optoelectronic memristors integrate the benefits of a wide bandwidth and ultra-high speed, providing opportunities and advantages for photonic computing and neuromorphic vision [13–16].

To date, several photosensitive materials have been used to construct optoelectronic memristor devices. For example, Lu et al. [17] prepared a transverse optoelectronic memristor based on $MAPbI_3$ materials, achieving device conductance reduction under optical stimulation and thus simulating the long-term depression behavior of synapses. Hu et al. [18] reported a ZnO_{1-x}/AlO_y double-layer optoelectronic memristor with light recognition, memory, and processing capabilities, demonstrating sustained photoconductivity properties under the action of light signals. Zhao et al. [19] developed an optoelectronic memristor device based on N-doped carbon points, adjusted the SET voltage of the device using ultraviolet light, and performed optically controlled reconfigurable logic calculations. However, the inherent

* Corresponding author (email: wangzq752@nenu.edu.cn, ycliu@nenu.edu.cn)
† These authors contributed equally to this work.

bandgap of photosensitive materials hinders their broad spectral response, which is not beneficial for mixed-color image recognition. Therefore, a novel optoelectronic memristor that can distinguish multi-wavelength light stimulation urgently needs to be developed.

The localized surface plasmon resonance (LSPR) effect, as an efficient interaction between light and matter, has attracted great interest in optoelectronic applications, including photocatalysis and optical detection [20,21]. In LSPR, the optical response wavelength is dominated by the morphology and size of metal nanoparticles distributed on a material's surface [22,23]. This tunability of the optical response can be exploited to overcome limitations associated with the inherent bandgap of the material. Therefore, leveraging the LSPR effect in an optoelectronic memristor may be an effective strategy for constructing a multi-wavelength optoelectronic memristor. In particular, constructing a metal/oxide interface with the appropriate potential barrier is necessary to achieve efficient separation of photogenerated electron-hole pairs [24, 25]. For an electrochemical metallization device, the oxidation of metal nanoparticles induced by the LSPR effect dominates the ion migration process under an electric field. The resulting multi-wavelength-modulated device is useful for constructing an artificial neural network (ANN) that can perform mixed-color pattern recognition. However, plasmonic optoelectronic memristors are still in their infancy, and few investigations have been reported.

In this study, we propose a multi-wavelength optoelectronic memristor based on silver (Ag)-titanium dioxide (TiO_2)/polymethyl methacrylate (PMMA) nanocomposite films using the LSPR effect. The resistive switching behaviors can be modulated using multi-wavelength light irradiation, in which the SET voltage gradually decreases. The formation/annihilation mechanism of Ag conductive filaments (CFs) has been verified by conductive atomic force microscopy (C-AFM) and temperature dependence measurements. Additionally, several logic operations have been demonstrated in the memristive circuits, including IMP and False gates. Furthermore, a mixed-color image recognition function has been implemented in a simulated ANN based on the optoelectronic memristor. The mixed-color image tests reveal a high recognition rate of 96.4%. The proposed multi-wavelength optoelectronic memristor has significant potential for application in efficient neuromorphic visual systems.

2 Experimental

Synthesis of Ag-TiO_2/PMMA composites. First, 0.5 g TiO_2 was immersed in 4 mol/L $AgNO_3$ solution and ultrasonicated for 2 h. Then the mixed dispersion was transferred to a petri dish and irradiated with UV light (310 nm). After a certain period of irradiation, the mixture was centrifuged, and pour out the supernatant. The remaining solids were centrifugally cleaned four times using deionized water, then transferred to a slide and placed in an oven at 60°C for 6 h. PMMA was dissolved in trichloromethane at a concentration of 5 mg/mL and ultrasonicated for 2 h. Then, different amounts of Ag-TiO_2 were added to the PMMA solution. The final Ag-TiO_2/PMMA suspensions with different concentrations were obtained by stirring in a centrifugal tube for 6 h.

Fabrication of the optoelectronic memristive device. Fluorine-doped tin oxide (FTO) glass was used as the substrate and the bottom electrode material. The Ag-TiO_2/PMMA suspensions were spun onto the FTO substrates at room temperature. Finally, the top Au electrodes were deposited by electron-beam evaporation.

Electrical measurements. The electrical measurements were performed using a source meter (2636A, Keithley). The optical modulation was performed using a xenon lamp (LA-410UV, Hayashi).

Implementation of spike-timing-dependent-plasticity (STDP). To implement STDP using Ag-TiO_2/PMMA-based plasmonic optoelectronic memristors, a series of single pulses were consecutively applied to the top electrode and bottom electrode. The first pulse was a negative voltage; then, positive pulses with decreasing amplitudes were subsequently applied. The timing interval $\Delta t > 0$ ($\Delta t < 0$) was defined as the interval between the end of the pre-synaptic (post-synaptic) spikes and the beginning of the post-synaptic (pre-synaptic) spikes. The post-synaptic conductance was measured in the dark state (G_0) and after 10 min visible light irradiation (G_1) with the paired spike. This represents the long-term plasticity of the synapse. The change in synaptic weight ΔW is defined as $(G_1 - G_0)/G_0$.

Calculation of accuracy. Structural similarity (SSIM) was employed to measure the difference between the learned image (x) and the input image (y). Here, high SSIM represents high learning accuracy. SSIM can be expressed as follows:

$$\mathrm{SSIM}(x, y) = f[l(x, y), c(x, y), s(x, y)], \tag{1}$$

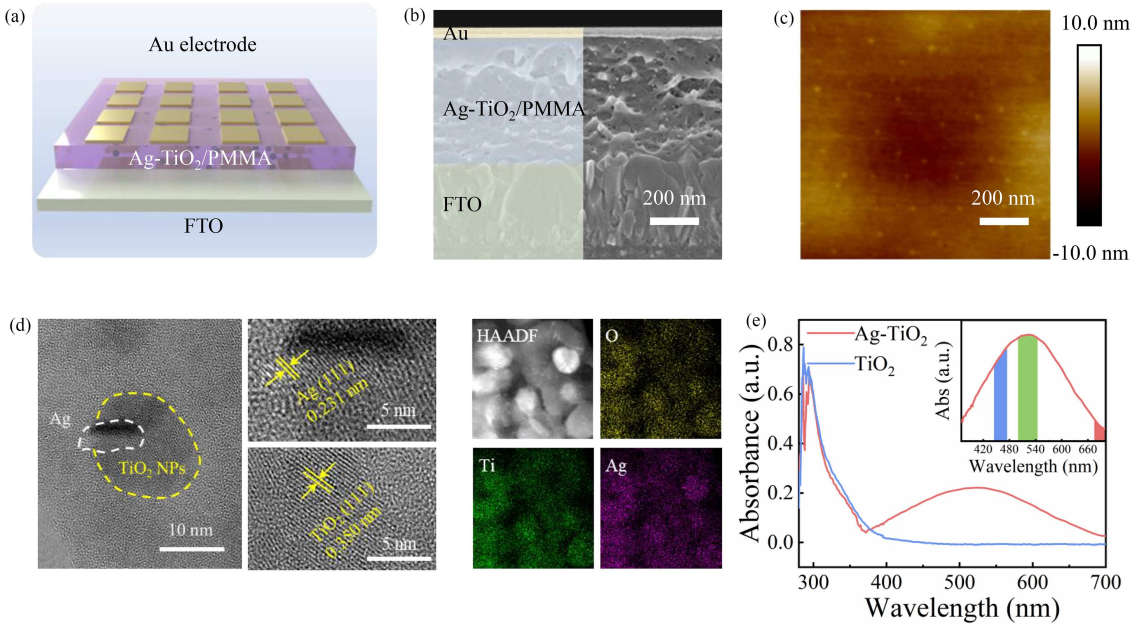

Figure 1 (Color online) Structural characterization of plasmonic optoelectronic memristor based on Ag-TiO_2/PMMA nanocomposite. (a) Illustration of the device, including Au top electrodes, Ag-TiO_2/PMMA films, and FTO bottom electrodes; (b) cross-sectional SEM image of the Au/Ag-TiO_2/PMMA/FTO memory device; (c) AFM image of the Ag-TiO_2/PMMA layer; (d) HRTEM images of the Ag-TiO_2 nanocomposite structures and elemental mapping images of the Ag-TiO_2/PMMA film; (e) absorption spectra of the Ag-TiO_2 film and a pure TiO_2 film. The inset shows the differential spectrum.

where $l(x, y)$, $c(x, y)$, and $s(x, y)$ are the brightness, contrast, and structure of the image, respectively. A detailed explanation of this metric can be found in [26].

3 Results and discussion

Figure 1(a) shows an illustration of the proposed plasmonic optoelectronic memristor device with an Au/Ag-TiO_2/PMMA/FTO structure. The Ag-TiO_2 nanoclusters were prepared by photocatalytic reduction in $AgNO_3$ solution, and the functional layer was fabricated by spin-coating (see more details in Section 2). As shown in Figure 1(b), the cross-sectional scanning electron microscopy (SEM) image indicates that the thickness of the Ag-TiO_2/PMMA nanocomposite layer is 650 nm. Corresponding top-view SEM images are shown in Figure S1(a). The top Au electrode with a diameter of 500 μm is deposited by high vacuum thermal evaporation. In addition, the surface morphology of the Ag-TiO_2/PMMA film has been characterized by AFM, as shown in Figure 1(c), confirming the high film quality. The Fourier transform infrared spectrum of Ag-TiO_2/PMMA is shown in Figure S1(b). The stretching vibrations of C=O and C-O bonds appear at 1716 and 1096 cm^{-1}, respectively. The stretching vibrations of C-H bonds in methyl and methylene groups show adsorption peaks at 2923 and 3008 cm^{-1} [27, 28]. The high-resolution transmission electron microscopy (HRTEM) images in Figure 1(d) further confirm that Ag and TiO_2 nanoparticles form nanocomposite structures. The lattice fringes at 0.231 and 0.350 nm correspond to the (111) plane of Ag and the (101) plane of anatase TiO_2, respectively [29, 30]. Furthermore, the right panel in Figure 1(d) shows the corresponding energy-dispersive X-ray mapping spectra, displaying the compositional distribution. To further investigate the structure of the Ag-TiO_2 nanoparticles, X-ray diffraction was performed, as shown in Figure S1(c). Diffraction peaks have been obtained for both TiO_2 (anatase phase) and Ag, further confirming the successful introduction of Ag in the composite film [31, 32]. Figure 1(e) shows the absorption spectra of TiO_2 and Ag-TiO_2 thin films. Compared with the TiO_2 films, a distinct absorption peak is observed in the visible region (centered at 535 nm) in Ag-TiO_2 films. According to the literature, this absorption peak can be attributed to the LSPR absorption properties of Ag nanoparticles [33–37].

The effects of visible light irradiation on the resistive switching (RS) behavior are investigated first. The devices with Ag-TiO_2 concentrations of 0.5 wt%, 1.0 wt%, and 1.5 wt% exhibit an abrupt transition between the high resistance state (HRS) and low resistance state (LRS) during the voltage sweep, as

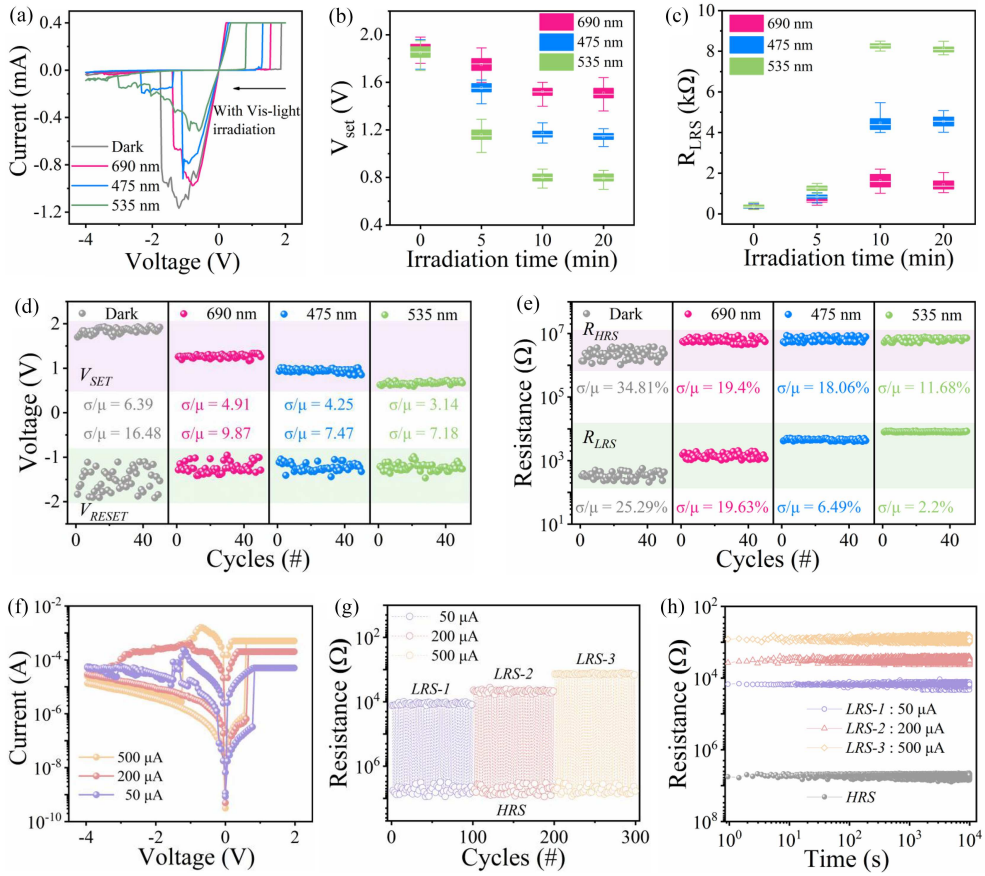

Figure 2 (Color online) Effects of visible light irradiation on resistive switching behaviors. (a) Typical RS behaviors after visible light irradiation of different light wavelengths. The values for (b) $V_{\rm SET}$ and (c) LRS resistance of different devices under visible light irradiation of different wavelengths. The data are collected from 50 consecutive RS cycles for each point after exposure to the given irradiation for 10 min. (d) The statistical results of the $V_{\rm SET}/V_{\rm RESET}$ and (e) $R_{\rm HRS}/R_{\rm LRS}$ values under continuous RS measurements after visible light irradiation of different light wavelengths. (f) Typical I-V characteristics of the device under CCs of 50, 200, and 500 μA. (g) Resistance values and (h) retention characteristics of multilevel resistance states with different CC values.

shown in Figure S2. To optimize the operation, the Ag-TiO_2 concentration of 1.5 wt% is selected for subsequent investigation. The I-V characteristics of Au/Ag-TiO_2/PMMA/FTO memory cells subjected to different wavelengths (red, 690 nm; green, 535 nm; and blue, 475 nm; with a power of 36 mW cm^{-2}) are measured, as shown in Figure 2(a). For the initial state without visible light exposure, a forming process is required to activate the device by applying a positive voltage (2.95 V) to the top electrode, and the device then exhibits typical bipolar resistive behavior (Figure S2). In contrast, the device abruptly switches on at the SET voltage of 0.8 V after employing visible light irradiation, indicating that the forming process is not required. Figures 2(b) and (c) show the $V_{\rm SET}$ and $R_{\rm LRS}$ values of the device during continuous cycle operation after visible light irradiation of different durations (0, 5, 10, and 20 min) and wavelengths (red, 690 nm; green, 535 nm; and blue, 475 nm; with a power of 36 mW cm^{-2}). Herein, $V_{\rm SET}$ decreases from 1.87 to 1.52, 1.13, and 0.79 V under visible light irradiation of 690, 475, and 535 nm, and $R_{\rm LRS}$ increases from 3×10^2 to 1.5×10^2, 4.5×10^3, and 8.1×10^3 Ω, respectively. Furthermore, when the irradiation is applied for 10 min, the $R_{\rm LRS}$ ($V_{\rm SET}$) value does not continue to increase (decrease), which may be due to saturation of the photoinduced oxidation in Ag nanoparticles. Therefore, we chose 10 min as the optimum pretreatment time. Figures 2(d) and (e) show the $V_{\rm SET}/V_{\rm RESET}$ and $R_{\rm HRS}/R_{\rm LRS}$ values collected during 50 consecutive switching cycles after visible light irradiation. $V_{\rm SET}/V_{\rm RESET}$ and $R_{\rm HRS}/R_{\rm LRS}$ exhibit negligible fluctuations, which means the stability of Au/Ag-TiO_2/PMMA/FTO memory devices can be improved after visible light irradiation. Furthermore, a more distinct increase/decrease in $R_{\rm LRS}$ and $V_{\rm SET}$ is obtained after visible light irradiation. The influence of the irradiation wavelength is consistent with the light absorption characteristics of the Ag-TiO_2/PMMA nanocomposite films. It is worth noting that the data overlap between these SET voltage values is not very significant, as shown in Figure S3. The

stable characteristics of device to device provide a guarantee for mixed-color image recognition. Moreover, multilevel storage behavior has been demonstrated by applying compliance currents (CCs) of 50, 200, and 500 μA. Figure 2(g) shows the differentiated resistance distributions obtained for 50 consecutive on-off cycles. As shown in Figure 2(h), all four resistance states exhibit negligible degradation within 10^4 s, indicating high retention ability. In addition, the mechanical flexibility of the memristor has been evaluated, and the electrical response of the memristor under different bending strains is shown in Figure S4. No significant degradation was observed in the resistivity under different bending strains, indicating that the Au/Ag-TiO_2/PMMA/FTO memory unit has effective bending resistance. Overall, our device presents broad application prospects in flexible neuromorphic vision systems.

We also consider the underlying memristive mechanism for multi-wavelength-modulated RS behaviors in our Ag-TiO_2/PMMA-based device. In Ag-TiO_2/PMMA nanocomposite films, the LSPR effect under visible light irradiation is accompanied by the generation of Ag^+, and Ag^+ migration occurs in an electric field. According to the ion migration model, the Ag^+ migration process is activated by heat, and the switching time is proportional to $\exp(-E_a/k_BT)$, where E_a is the activation energy of ion migration, k_B is the Boltzmann constant, and T is temperature [38, 39]. Herein, Ag-TiO_2/PMMA memory cells in the initial state and after 10 min of visible light irradiation were used for comparison. Temperature-dependent SET measurements are performed in the pulsed program mode (as shown in Figure S5(a)), with and without visible light exposure for 10 min, to determine E_a values. The SET curves in the initial state and after 10 min of irradiation are shown in Figure S5, and the corresponding switching times (Δt) depending on temperature are shown in Figures 3(a) and (b), respectively. A linear relationship between the $\ln(\Delta t)$ and $1/k_BT$ curves is obtained, for which the E_a values are 0.67 and 0.48 eV in the initial dark state and after 10 min of visible light irradiation, respectively. Therefore, the LSPR effect reduces the migration barrier of Ag^+, which is responsible for the lower V_{SET} value [40, 41]. To better understand the physical mechanism of the light-modulated RS behavior, we perform C-AFM, as shown in Figures 3(c) and (d). In the initial dark state, the entire surface area exhibits a relatively low current value, representing the HRS. In a dark environment, a locally bright region is obtained after applying a SET voltage, indicating the formation of strong CFs (Figure S6). Under visible light irradiation at 535 nm, a thinner CF is formed, as shown in Figure 3(d). On this basis, a possible switching model is proposed, as shown in Figures 3(e) and (f). In the LRS, Ag CFs are formed through the oxidation, migration, and reduction of Ag under an electric field. Meanwhile, the LSPR effect effectively promotes the generation of Ag^+ and reduces the SET voltage when exposed to visible light, thus inhibiting the uncontrollable growth of CFs.

Next, memristive logic circuits have been designed to further evaluate the application of our device. As depicted in Figure 4(a), the IMP logic circuit consists of two RRAM devices, namely P and Q, which are connected to the ground using a 10^4 Ω resistor R_L (LRS $\ll R_L \ll$ HRS). Here, we define two beams of incident light with intensities of 0 and 36 mW cm^{-2} as input light 0 and 1, respectively. The current values corresponding to HRS and LRS (monitored by electrical pulse 0.2 V/1 ms) are defined as logical output 0 and 1, respectively. Considering the switching voltage and the voltage distribution over the R_L, the electrical pulses applied to devices P and Q are set as 0.9 V/1 ms and 2 V/1 ms, respectively. For the IMP operation, devices P and Q are initialized to HRS. In the input process, the method of simultaneous input is adopted. After two beams of visible light are irradiated, V_P (0.9 V/1 ms) and V_Q (2 V/1 ms) are simultaneously applied to the memristor. Then the output results are read by electrical pulses of 0.2 V. If the devices P and Q are written 0 and 0, the device Q will change to LRS after the IMP operation, obtaining the logic 1. If the devices P and Q are written 1 and 0, the voltage drop on device Q cannot make the device switch from the HRS to LRS when device P is in the LRS. When the devices P and Q are written 1 and 1, the devices P and Q are almost simultaneously transformed into LRS, resulting in the output of 1. The logic output is consistent with the truth result of IMP, indicating that the IMP operation has been successfully implemented (Figure 4(b)). Figure 4(c) shows the False logic operation achieved with the assistance of 475 and 690 nm light (36 mW cm^{-2}). For False logic instructions, devices P and Q cannot switch to the LRS by applying V_P (0.9 V/1 ms) or V_Q (0.9 V/1 ms) under 475 and 690 nm light. Then, the output results are read by electrical pulses of 0.2 V. The measured logic results and true values are shown in Figure 4(d); the output states can be stably retained and stored, enabling non-volatile stateful reconfigurable logic.

On the basis of the variation in the photoresistive characteristics of the memristor, time-resolved current measurements are carried out at two wavelengths and under positive bias, as shown in Figure 4(e). In this configuration, the electrical signal and the optical signals of 690 and 535 nm serve as input signals a,

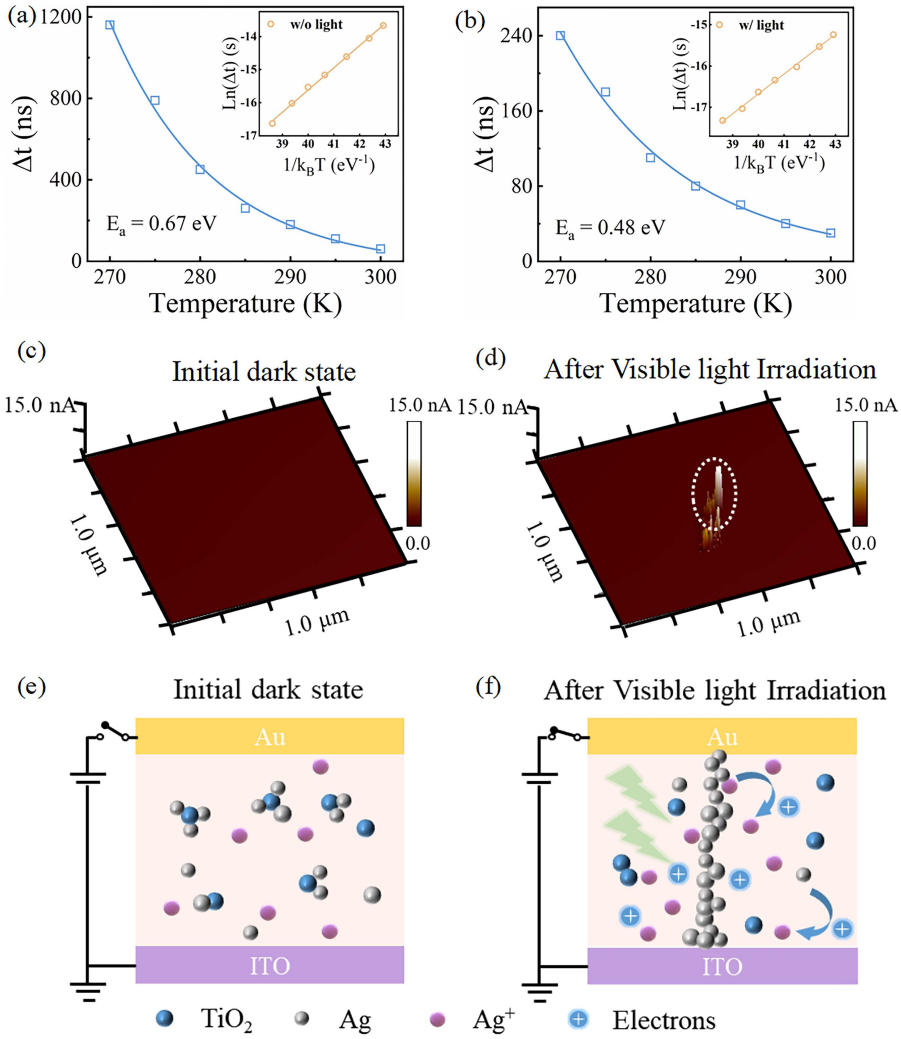

Figure 3 (Color online) RS mechanism of Au/Ag-TiO_2/PMMA/FTO memristors. (a) and (b) Temperature dependence of SET switching time for the memristor without and with 535 nm light irradiation. The Arrhenius plots used for determining the migration barrier energy are shown in the insets. Local conductivity of the Au/Ag-TiO_2/PMMA/FTO memristor measured by C-AFM (10 mV bias) for (c) the initial state and (d) the LRS after SET operation using 535 nm light irradiation. Illustrations of the switching mechanism of the Au/Ag-TiO_2/PMMA/FTO memory devices in (e) the initial state and (f) the LRS after SET operation with 535 nm light irradiation.

b, and *c*, respectively. For electrical input, the input conditions of 0.9 V/1 ms and 1.7 V/1 ms represent logic 0 and 1, respectively. As for the optical input (690 and 535 nm), the off and on states are set as 0 and 1, respectively. The current values corresponding to the HRS and LRS of the optoelectronic memristor are defined as 0 and 1 (denoted as *Y*), respectively. Output currents above and below a threshold current of 1 μA are defined as 1 and 0, respectively. As shown in the truth table (Figure 4(f)), when the input signals of *a*, *b*, and *c* are 00001111, 00110011, and 01010101, the output signal of *Y* is 01010111. Therefore, the logic operation can be achieved in a single device (Figure 4(g)). In previous studies, at least two transistors were required for the logic operations [42–45]. Consistent with our previous results, the multi-wavelength plasmonic optoelectronic memristor exhibits great potential in reconfigurable logic circuits.

To demonstrate visual multifunctional integration, we design a neuromorphic vision system using an optoelectronic memristor to implement image preprocessing and pattern recognition (Figure 5(a)). In this system, the optoelectronic memristor array serves as the preprocessing module to extract and store wavelength information. Meanwhile, the memristive neural network performs the image recognition function, to recognize the red, green, and blue (RGB) information. Figure 5(b) illustrates the preprocessing results for the RGB mixed-color images (represented using numbers 1–6). The multi-wavelength information can be distinguished using different SET voltages. As plotted in the left panel, only the memristive device

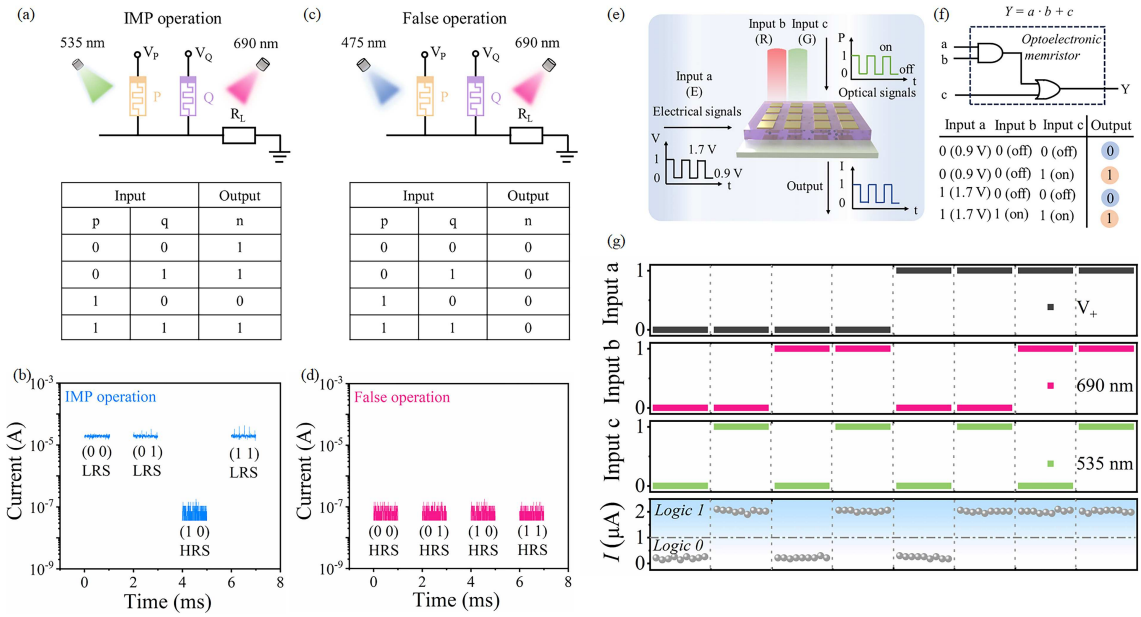

Figure 4 (Color online) Optoelectric logic operating with multiple optical input sources. (a) Circuit and truth table for IMP operation. (b) Readout current of RRAM devices P and Q after the IMP operation. (c) Circuit and truth table for False operation. (d) Readout current of devices P and Q after False operation. (e) and (f) Basic operation principle and schematic of the logic circuit for logical operation based on Ag-TiO_2/PMMA-based plasmonic optoelectronic memristor devices. The nonlinear output current is programmed by 690 and 535 nm light signals and electrical pulses. (g) Output current responses of the optoelectronic three-input logic application.

irradiated with green light can be switched to the LRS under the SET voltage of 0.9 V. In contrast, the SET voltage of 1.7 V is required to realize RS behavior under red light irradiation. Then, the feature information is sent to the ANN for subsequent image recognition. Note that the STDP rule is adopted as a common learning rule to implement color image recognition [46,47]. For the STDP learning rule, the synaptic weight changes (ΔW) are dominated by the interval between pre-synaptic and post-synaptic spikes. Herein, the synaptic weight is defined as $\Delta W = (G_1 - G_0)/G_0$, where G_0 and G_1 represent the initial and stable conductance after electrical pulses, respectively. Detailed information regarding the STDP measurement is presented in Section 2. As shown in Figure 5(c), visible light irradiation enhances the synaptic weight change to a different extent, in which the greater ΔW is obtained with green light irradiation. Accordingly, mixed-color image recognition is demonstrated in our memristive neural network. The input image is composed of 56×56 pixels. Figure 5(d) shows the evolution of images with different training numbers during the original transformation of the image and the learning process after using Gaussian noise. The dependence of the recognition accuracy with and without Gaussian noise on the number of training epochs is plotted in Figure 5(e). After 400 training epochs, the learning accuracy of the neural network based on the Ag-TiO_2/PMMA photoelectric memristor device reaches 96.4%. Meanwhile, the recognition accuracy can still exceed 89.5% under Gaussian noise with a mean of 0 and a variance of 0.1. In addition, different noise levels are used to demonstrate its anti-interference ability, as shown in Figure S8. The results show that the feature information is effectively extracted during the preprocessing of the optoelectronic memristor array, resulting in high-precision color pattern recognition.

4 Conclusion

In this study, we have developed a multi-wavelength identifiable memristor device based on Ag-TiO_2/PMMA nanocomposites. In particular, multilevel storage has been realized using visible light irradiation of different wavelengths. The multi-wavelength modulation characteristics can be attributed to the photoinduced oxidation of Ag nanoparticles. The photoinduced oxidation process promotes Ag^+ migration under an electric field and reduces the SET voltage. Furthermore, IMP and False logic operations have been demonstrated by combining electrical and optical signals in our memristive circuits. Finally, neuromorphic preprocessing and recognition of mixed-color images have been realized in simulated ANNs. The

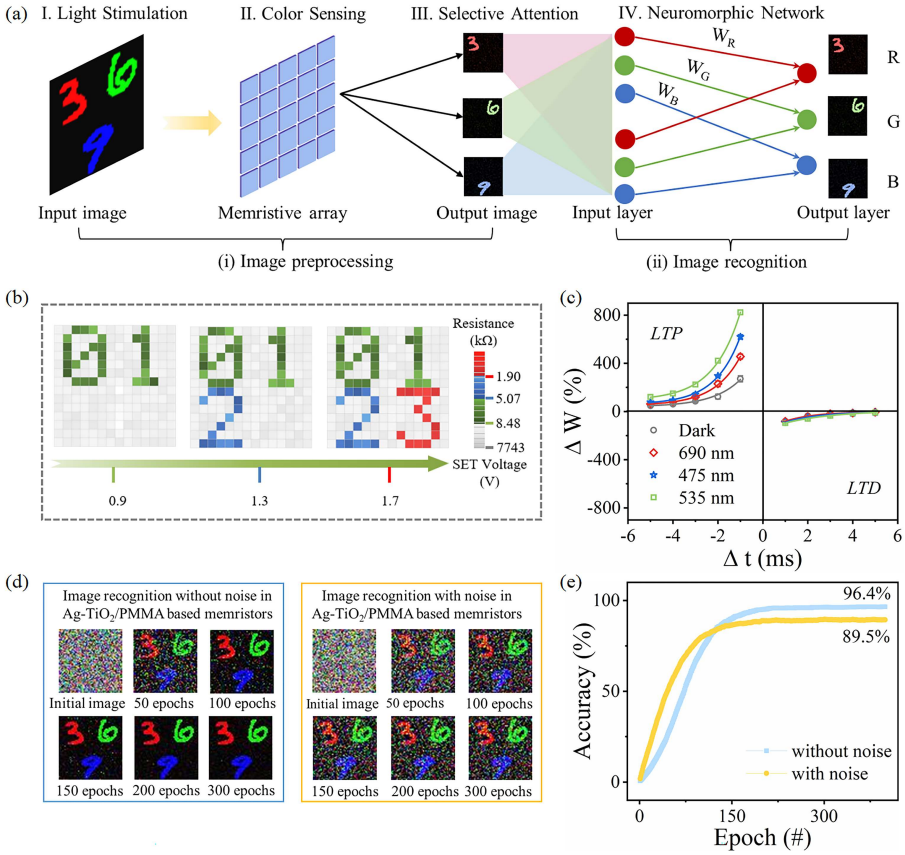

Figure 5 (Color online) Mixed-color pattern recognition in the Ag-TiO_2/PMMA optoelectronic memristor-based neuromorphic visual system. (a) Illustration of the neuromorphic vision system, which contains the image preprocessing and recognition parts based on visual attention and STDP synaptic weight updating; (b) color recognition preprocessed by the memristor array; (c) synaptic weight variation (ΔW) versus relative spike timing (Δt), showing typical STDP characteristics, similar to biological synapses; (d) evolution of the images during the learning processes without noise and with noise in Ag-TiO_2/PMMA-based memristors; (e) recognition accuracy as a function of the learning epochs used for the memristive ANN.

neuromorphic preprocessing function reduces redundant data and provides high recognition accuracy. The proposed plasmon optoelectronic devices show great prospects in the field of logic calculation and neuromorphic vision.

Acknowledgements This work was financially supported by Ministry of Science and Technology of China (Grant No. 2023YFB-4402301), National Science Fund for Distinguished Young Scholars (Grant No. 52025022), National Natural Science Foundation of China (Grant Nos. 11974072, U19A2091, 52372137, U23A20568, 62004016, 52272140, 52072065), China Postdoctoral Science Foundation (Grant No. GZB20240135), Funds from Jilin Province (Grant No. 20230402072GH), and Fundamental Research Funds for the Central Universities (Grant No. 2412023YQ004).

Supporting information Figures S1–S8. The supporting information is available online at info.scichina.com and link.springer.com. The supporting materials are published as submitted, without typesetting or editing. The responsibility for scientific accuracy and content remains entirely with the authors.

References

1 Bez R, Pirovano A. Non-volatile memory technologies: emerging concepts and new materials. Mater Sci Semicond Process, 2004, 7: 349–355
2 Bez R, Camerlenghi E, Modelli A, et al. Introduction to flash memory. Proc IEEE, 2003, 91: 489–502
3 von Neumann J. The principles of large-scale computing machines. IEEE Ann Hist Comput, 1988, 10: 243–256
4 Liu Q, Yue W, Li Y, et al. Multifunctional optoelectronic random access memory device based on surface-plasma-treated inorganic halide perovskite. Adv Elect Mater, 2021, 7: 2100366
5 Jo S H, Chang T, Ebong I, et al. Nanoscale memristor device as synapse in neuromorphic systems. Nano Lett, 2010, 10: 1297–1301
6 Sun L, Wang Z, Jiang J, et al. In-sensor reservoir computing for language learning via two-dimensional memristors. Sci Adv, 2021, 7: eabg1455
7 Xiang D, Liu T, Xu J, et al. Two-dimensional multibit optoelectronic memory with broadband spectrum distinction. Nat Commun, 2018, 9: 2966
8 He J, Wei R, Ge S, et al. Artificial visual-tactile perception array for enhanced memory and neuromorphic computations. InfoMat, 2024, 6: e12493
9 Yu S, Chen H Y, Gao B, et al. HfO_x-based vertical resistive switching random access memory suitable for bit-cost-effective three-dimensional cross-point architecture. ACS Nano, 2013, 7: 2320–2325

10 Wu M-C, Ting Y-H, Chen J-Y, et al. Low power consumption nanofilamentary ECM and VCM cells in a single sidewall of high-density VRRAM arrays. Adv Sci, 2019, 6: 1902363
11 Urquiza M L, Islam M M, van Duin A C T, et al. Atomistic insights on the full operation cycle of a HfO_2-based resistive random access memory cell from molecular dynamics. ACS Nano, 2021, 15: 12945–12954
12 Yin C, Gong C, Tian S, et al. Low-energy oxygen plasma injection of 2D Bi_2Se_3 realizes highly controllable resistive random access memory. Adv Funct Mater, 2022, 32: 2108455
13 Tan H, Zhou Y, Tao Q, et al. Bioinspired multisensory neural network with crossmodal integration and recognition. Nat Commun, 2021, 12: 1120
14 Wang W, Gao S, Li Y, et al. Artificial optoelectronic synapses based on TiN_xO_{2-x}/MoS_2 heterojunction for neuromorphic computing and visual system. Adv Funct Mater, 2021, 31: 2101201
15 Ahmed T, Tahir M, Low M X, et al. Fully light-controlled memory and neuromorphic computation in layered black phosphorus. Adv Mater, 2021, 33: 2004207
16 Zheng J, Du Y, Dong Y, et al. Fully light-modulated memristor based on ZnO/MoO_x heterojunction for neuromorphic computing. Appl Phys Lett, 2024, 124: 133502
17 Zhu X, Lu W D. Optogenetics-inspired tunable synaptic functions in memristors. ACS Nano, 2018, 12: 1242–1249
18 Hu D C, Yang R, Jiang L, et al. Memristive synapses with photoelectric plasticity realized in ZnO_{1-x}/AlO_y heterojunction. ACS Appl Mater Interfaces, 2018, 10: 6463–6470
19 Xu J, Wang X, Zhao X, et al. Light-controlled stateful reconfigurable logic in a carbon dot-based optoelectronic memristor. Appl Phys Lett, 2024, 124: 073507
20 Li Z, Zi J, Luan X, et al. Localized surface plasmon resonance promotes metal-organic framework-based photocatalytic hydrogen evolution. Adv Funct Mater, 2023, 33: 2303069
21 Zhang L, Ding N, Lou L, et al. Localized surface plasmon resonance enhanced photocatalytic hydrogen evolution via Pt@Au NRs/C_3N_4 nanotubes under visible-light irradiation. Adv Funct Mater, 2019, 29: 1806774
22 Hutter E, Fendler J H. Exploitation of localized surface plasmon resonance. Adv Mater, 2004, 16: 1685–1706
23 Mayer K M, Hafner J H. Localized surface plasmon resonance sensors. Chem Rev, 2011, 111: 3828–3857
24 Chen J J, Wu J C S, Wu P C, et al. Improved photocatalytic activity of shell-isolated plasmonic photocatalyst $Au@SiO_2/TiO_2$ by promoted LSPR. J Phys Chem C, 2012, 116: 26535–26542
25 Liu M, Kang Q, Xie Z, et al. Heterostructure nanocomposite with local surface plasmon resonance effect enhanced photocatalytic activity—a critical review. J Phys D-Appl Phys, 2022, 55: 043002
26 Wang Z, Bovik A C, Sheikh H R, et al. Image quality assessment: from error visibility to structural similarity. IEEE Trans Image Process, 2004, 13: 600–612
27 Abdollahi H, Najafi V, Amiri F. Determination of monomer reactivity ratios and thermal properties of poly(GMA-co-MMA) copolymers. Polym Bull, 2021, 78: 493–511
28 Taha R H, Taha T H, Abu-Saied M A, et al. Successful production of bioethanol from olive waste residues followed by its purification using poly (acrylonitrile-co-methylacrylate)/polymethylmethaacrylate membrane. Biomass Conv Bioref, 2023, 13: 16115–16129
29 Ling L, Bai Y, Li Y, et al. Quick activation of nanoporous anatase TiO_2 as high-rate and durable anode materials for sodium-ion batteries. ACS Appl Mater Interfaces, 2017, 9: 39432–39440
30 Ma C, Wang X, Luo H, et al. Synthesis of Ag/TiO_2 core-shell nanowires with enhanced stability of photocatalytic activity. J Mater Sci-Mater Electron, 2017, 28: 10715–10719
31 Zhou W, Sun F, Pan K, et al. Well-ordered large-pore mesoporous anatase TiO_2 with remarkably high thermal stability and improved crystallinity: preparation, characterization, and photocatalytic performance. Adv Funct Mater, 2011, 21: 1922–1930
32 Kunnamareddy M, Diravidamani B, Rajendran R, et al. Synthesis of silver and sulphur codoped TiO_2 nanoparticles for photocatalytic degradation of methylene blue. J Mater Sci-Mater Electron, 2018, 29: 18111–18119
33 Li X, Fu S, Wang X, et al. Enhancing hologram memory via deposition of plasmonic nanocubes on orderly mesoporous titania. Opt Express, 2020, 28: 13008
34 Fu S, Zhang X, Han R, et al. Photoinduced anisotropy and polarization holographic gratings formed in Ag/TiO_2 nanocomposite films. Appl Opt, 2012, 51: 3357
35 Wang X, Fu S, Zhang X, et al. Visible laser-assisted reduction of plasmonic Ag nanoparticles with narrow-band optical absorption for colored holographic reconstruction. Opt Express, 2017, 25: 31253
36 Wang X, Fu S, Zhang X, et al. Bi-photonic reduction of anisotropic Ag nanoparticles for color-tunable hologram reconstruction. Opt Express, 2019, 27: 11991
37 Shan X, Zhao C, Wang X, et al. Plasmonic optoelectronic memristor enabling fully light-modulated synaptic plasticity for neuromorphic vision. Adv Sci, 2022, 9: 2104632
38 Nayak A, Tamura T, Tsuruoka T, et al. Rate-limiting processes determining the switching time in a Ag_2S atomic switch. J Phys Chem Lett, 2010, 1: 604–608
39 Calderon V S, Galindo R E, Benito N, et al. Ag^+ release inhibition from ZrCN-Ag coatings by surface agglomeration mechanism: structural characterization. J Phys D-Appl Phys, 2013, 46: 325303
40 Waser R, Aono M. Nanoionics-based resistive switching memories. Nat Mater, 2007, 6: 833–840
41 Han J, Shan X, Lin Y, et al. Multi-wavelength-recognizable memristive devices via surface plasmon resonance effect for color visual system. Small, 2023, 19: 2207928
42 Dathbun A, Kim Y, Kim S, et al. Large-area CVD-grown sub-2 V ReS_2 transistors and logic gates. Nano Lett, 2017, 17: 2999–3005
43 Yu L, El-Damak D, Radhakrishna U, et al. Design, modeling, and fabrication of chemical vapor deposition grown MoS_2 circuits with E-mode FETs for large-area electronics. Nano Lett, 2017, 16: 6349–6356
44 Lin Z, Liu Y, Halim U, et al. Solution-processable 2D semiconductors for high-performance large-area electronics. Nature, 2018, 562: 254–258
45 Zhang Y, Wang L, Yang M, et al. Multiposition controllable gate WS_2/MoS_2 heterojunction phototransistor and its applications in optoelectronic logic operation and emulation of neurotransmission. Adv Opt Mater, 2022, 10: 2200197
46 Kim S, Choi B, Lim M, et al. Pattern recognition using carbon nanotube synaptic transistors with an adjustable weight update protocol. ACS Nano, 2017, 11: 2814–2822
47 Lin Y, Wang C, Ren Y, et al. Analog-digital hybrid memristive devices for image pattern recognition with tunable learning accuracy and speed. Small Methods, 2019, 3: 1900160

Profile of Yichun LIU

Prof. Yichun LIU is currently a professor of Optoelectronic Functional Materials and Devices at Northeast Normal University. He obtained his B.Sc. from Northeast Normal University in 1985 and his Ph.D. from the Changchun Institute of Optics, Fine Mechanics and Physics, Chinese Academy of Sciences and Politecnico di Torino (Italy) in 1995.

Prof. Yichun LIU is an academician of the Chinese Academy of Sciences, the director of the Key Laboratory for UV Light-Emitting Materials and Technology of the Ministry of Education, the vice chairman of the Jilin Provincial Association for Science and Technology, a member of the International Conference on Luminescence (ICL) Program Committee, and the Advisory Committee of the International Conference on II-VI Compound Materials.

His research interests include optical/electronic memory, wide-band-gap semiconductors, and short-wavelength light-emitting devices.

Prof. Yichun LIU is a recipient of the National Science Fund for Distinguished Young Scholars and Chinese Academy of Sciences Hundred Talents Program. He won the second prize of the National Natural Science Award (ranked first) twice in 2015 and 2019.

Selected publications

• Miao J Y, Fu S C, Zhang S, et al. Robust carbon-dot optical disks for orthogonal amplitude-polarization encryption storage. Laser Photonics Rev, 2024. doi: 10.1002/lpor.202401231

• Shan X Y, Zhao C Y, Wang X N, et al. Plasmonic optoelectronic memristor enabling fully light-modulated synaptic plasticity for neuromorphic vision. Adv Sci, 2022, 9: 2104634

• Zhao X N, Xu J Q, Xie D, et al. Natural acidic polysaccharide-based memristors for transient electronics: highly controllable quantized conductance for integrated memory and nonvolatile logic applications. Adv Mater, 2021, 33: 2104023

• Zhou Y, Qin Z, Liang Z Z, Ultra-broadband metamaterial absorbers from long to very long infrared regime. Light Sci Appl, 2021, 10: 138

• Ielmini D, Wang Z Q, Liu Y C, Brain-inspired computing via memory device physics. APL Mater, 2021, 9: 050702

• Wang Y Q, Li X, Fu S C, et al. Nondestructive readout of holographic memory in Ag/TiO_2 heterojunction via carbon-dots and hydrogel co-modification. Appl Phys Lett, 2021, 118: 141601

• Lin Y, Liu J L, Shi J J, et al. Nitrogen-induced ultralow power switching in flexible ZnO-based memristor for artificial synaptic learning. Appl Phys Lett, 2021, 118: 103502

• Wang Z Q, Zeng T, Ren Y Y, et al. Toward a generalized Bienenstock-Cooper-Munro rule for spatiotemporal learning via triplet-STDP in memristive devices. Nat Commun, 2020, 11: 1510

• Zhao X N, Wang Z Q, Li W T, et al. Photoassisted electroforming method for reliable low-power organic-inorganic perovskite memristors. Adv Funct Mater, 2020, 30: 1910151

• Yao Y, Wang Z Q, Xu H Y, et al. Moisture-powered memristor with interfacial oxygen migration for power-free reading of multiple memory states. Nano Energy, 2020, 71, 104628

• Wu J R, Fu S C, Zhang X T, et al. Bidirectional photochromism via anchoring of carbon dots to TiO_2 porous films. ACS Appl Mater Interfaces, 2020, 12: 6262–6267

• Wang H T, Yang M H, Tang Q X, et al. Flexible, conformal organic synaptic transistors on elastomer for biomedical applications. Adv Funct Mater, 2019, 29: 1901107.

• Zhao X N, Wang Z Q, Xu H Y, et al. Memristors with organic-inorganic halide perovskites. InfoMat, 2019, 1: 183–210

• Liu S Y, Fu S C, Zhang X T, et al. UV-resistant holographic data storage in noble-metal/semiconductor nanocomposite films with electron-acceptors. Opt Mater Express, 2018, 8: 1143–1153

• Wang Z Q, Xu H Y, Li X H, et al. Synaptic learning and memory functions achieved using oxygen ion migration/diffusion in an amorphous InGaZnO memristor. Adv Funct Mater, 2012, 22: 2759–2765